J Mater Sci (2008) 43:2631–2641
DOI 10.1007/s10853-008-2480-x

Microstructure and phase transformation of zirconia-based ternary oxides for thermal barrier coating applications

Xiao Huang · Andrey Zakurdaev · Dongmei Wang

Received: 6 August 2007 / Accepted: 18 January 2008 / Published online: 19 February 2008

Abstract Five dopant oxides, Sc_2O_3, Yb_2O_3, CeO_2, Ta_2O_5, and Nb_2O_5, were incorporated into 7YSZ to create ternary zirconia-based oxides with varying oxygen vacancies and substitutional defects. These ternary oxides were consolidated using a high-temperature sintering process. The resulting bulk oxides were subjected to microstructural study using scanning electron microscopy (SEM), X-ray diffraction (XRD), and differential scanning calorimetry (DSC). The results show that the microstructures of the ternary zirconia-based oxides are determined by the amount of oxygen vacancies in the system, the dopant cation radius, and atomic mass. Increasing the number of oxygen vacancies in the lattice by the addition of trivalent dopant as well as the use of larger cations promotes the stabilization of the high-temperature cubic phase. The tetravalent cation, on the other hand, has the effect of retaining tetragonal phase to room temperature without the influence of oxygen vacancy. The addition of pentavalent oxide leads to the formation of monoclinic phase upon cooling.

Introduction

Thermal barrier coatings (TBCs) play an important role in protecting superalloy substrate components in gas turbine engines from reaching excessive temperatures. Typically, the metal surface temperature can be reduced by as much as 150 °C with the application of zirconia-based TBCs. The actual temperature reduction is also influenced by the coating thickness and cooling scheme used. Continuous development of new TBC materials and structures is driven by the demand for higher turbine inlet temperature, as an effective means to enable higher gas turbine efficiency and reduced greenhouse gas emissions. The primary requirements for the new coating materials are lower thermal conductivity, increased durability for operation at higher temperatures, and compatibility with the bond coat and substrate superalloys.

Since pure zirconia experiences a phase transformation from tetragonal (*t*) phase to monoclinic (*m*) phase during cooling, thermal stresses and subsequent crack formation can be initiated by the volume changes related to the phase transformation. For this reason, various metal oxides (or dopants), such as CaO, MgO, CeO_2, Sc_2O_3, and Y_2O_3, have been added to ZrO_2 in order to stabilize or partially stabilize either cubic (*c*) or tetragonal (*t*) phase to room temperature [1]. Among these metal oxides, Y_2O_3 has been regarded to be the most suitable dopant to stabilize ZrO_2 for TBC applications [2–4] since YSZ exhibits comparatively low thermal conductivity, superior mechanical properties and compatibility to the MCrAlY or aluminide bond-coat than ZrO_2 stabilized by other dopants. The optimum amount of yttria added to zirconia was found to be near 7–8 wt.% (4–4.5 mol%), with this composition offering the highest degree of resistance to coating spallation and improved thermal stability [5, 6].

In addition to the phase stabilization effect, the incorporation of dopants can create more phonon scattering centers and reduce the thermal conductivity of the zirconia-based TBCs. It has been observed that the thermal conductivities for ternary systems, based on 4 mol% Y_2O_3–4 mol% of Yb_2O_3, Er_2O_3, Gd_2O_3, or Nd_2O_3–ZrO_2, were significantly lower than the thermal conductivities measured for binary

X. Huang (✉) · A. Zakurdaev · D. Wang
Department of Mechanical and Aerospace Engineering,
Carleton University, 1125 Colonel By Drive, Ottawa, ON,
Canada K1S 5B6
e-mail: xhuang@mae.carleton.ca

YSZ [7]. Multiple component oxide systems, Nd_2O_3 (Gd_2O_3, Sm_2O_3)-Yb_2O_3 (Sc_2O_3) co-doped zirconia-yttria or hafnia-yttria, have been shown to be very effective in reducing thermal conductivity and enhancing high-temperature phase stability [8]. Highly defective lattice structures with nano-scaled defect clusters were observed in the multiple component oxide systems. While the improved performance can be correlated to the amount of dopants and their types, fundamentally the microstructure, including phase compositions and chemistry in each phase, determines the properties of the TBC materials [9]. Although the binary ZrO_2–Y_2O_3 system has been extensively studied [10], the microstructure and phase transformations of ternary and higher orders of zirconia-based oxide systems are not well understood. Depending on the type and percentage of the dopant(s) and the heat treatment history, ZrO_2-based materials can assume monoclinic (*m*), tetragonal (*t*), and/or cubic (*c*) crystal structures at a given temperature. The present research was initiated to study the microstructure and the relationship between microstructure and thermal and mechanical properties of ternary zirconia-based ceramic materials. In our previous study, the effect of dopant addition on the thermal conductivity of ternary ZrO_2-based materials was reported [9]. In this study, the microstructure and phase transformation of ternary metal oxide co-doped yttria-stabilized zirconia systems were evaluated. 7YSZ (3.945 mol% Y_2O_3–ZrO_2) was used as the base material and co-doped by oxides with varying valence, ionic mass, and radius to achieve predetermined amounts of oxygen vacancies and substitutional point defects. Fully dense materials were fabricated, microstructures evaluated at room temperature, and phase transformations studied during subsequent heating and cooling cycles.

Materials and experimental methods

Materials

The co-dopant oxides selected for this study and their properties are given in Table 1. The purities of all materials were greater than 99.9%. Scandium oxide (Sc_2O_3) and ytterbium oxide (Yb_2O_3) (Yb^{3+} having larger radius and mass than Sc^{3+}) were selected to substitute Zr^{4+} in the 7YSZ lattice structure and create additional oxygen vacancies. To examine the effect of co-dopant without the influence of oxygen vacancies, tetravalent cerium oxide (CeO_2) was added to 7YSZ. Pentavalent oxides, tantalum pentoxide (Ta_2O_5), and niobium pentoxide (Nb_2O_5) were used to eliminate the influence of oxygen vacancies in 7YSZ since the oxygen vacancies created by Y^{3+} can be annihilated by the addition of pentavalent cations in equal mole percentages to trivalent cations. Since Ta^{5+} has similar ionic radii as Nb^{5+} but double the mass, the effect of dopant atomic mass on the microstructure can be studied as well. The amount of co-dopant addition in each sample is given in Table 2. The sample ID of ternary oxide was determined based on the rounded molar percent of co-dopant cation in 7YSZ. Also included in the table is the composition of 7YSZ. 7YSZ was examined in this study to provide a baseline for comparison.

Table 1 Characteristics of selected metal oxides as co-dopant to 7YSZ

Co-dopant	Cation	Atomic mass	Ionic radius (nm)	Suppliers
Y_2O_3 (dopant)	Y^{3+}	88.91	0.089	Praxair
Sc_2O_3	Sc^{3+}	44.96	0.072	Metall Rare Earth Ltd.
Yb_2O_3	Yb^{3+}	173.04	0.086	Metall Rare Earth Ltd.
CeO_2	Ce^{4+}	140.11	0.092	Metall Rare Earth Ltd.
Ta_2O_5	Ta^{5+}	180.95	0.068	Metall Rare Earth Ltd.
Nb_2O_5	Nb^{5+}	92.91	0.069	Sigma–Aldrich
ZrO_2 (Host)	Zr^{4+}	91.22	0.079	Praxair

Material fabrication

The powder materials were blended according to the compositions given in Table 2. Ball milling method was selected to alloy the powder material since it is simple, effective, and has shown success in achieving complete solid solution after 24-h milling time [11, 12]. ZrO_2 balls with density of 6.27 g/cm^3 and ball diameter of 10 mm were used as the grinding media. After 20 h milling, the alloyed powders were compacted uniaxially at 200 MPa to form 2–4 mm thick and 15 mm diameter disks. A sintering temperature of 1,500 °C was used in this study. The sintering time was calculated based on the longest distance, determined by the powder particle size, the cations have to travel in order to achieve homogeneous compositions. The selected sintering time of 120 h allows cations to travel a distance of 7 μm [13] at 1,500 °C. After sintering, the samples were furnace cooled to room temperature at a cooling rate of ~5 °C/min.

Microstructure characterization

A scanning electron microscope (SEM) (Hitachi S-570 SEM) was employed in this study to evaluate the surface morphologies and cross-sectional microstructures of the as-sintered samples. The grain size was determined using a

Table 2 Compositions of co-doped 7YSZ

Sample ID	Targeted co-dopant mol% (per 100 mol% 7SYZ)	Final co-dopant cation mol% (per 100 cations)	Final Y^{3+} mol% (per 100 cations)
7YSZ	3.945 mol% Y_2O_3		7.59
5ScYSZ	2.5 mol% Sc_2O_3	4.71 (Sc^{3+})	7.23
5YbYSZ	2.5 mol% Yb_2O_3	4.71 (Yb^{3+})	7.23
5CeYSZ	5 mol% CeO_2	4.71 (Ce^{4+})	7.23
7TaYSZ	3.945 mol% Ta_2O_5	7.05 (Ta^{5+})	7.06
7NbYSZ	3.945 mol% Nb_2O_5	7.05 (Nb^{5+})	7.06

Clemex Vision PE 4.0 Image Analysis System (Clemex Technologies, Inc) while the bulk densities of the co-doped zirconia-based ceramic samples were measured using Archimedes' method.

The phase compositions in the sintered samples were characterized by X-ray diffraction (XRD) technique. Prior to XRD analysis, the sintered samples were manually polished using diamond paste to achieve a smooth surface and expose internal bulk material. The types of phases present were determined by comparing the XRD patterns of the samples with a reference database. The percentages of various phases were calculated using relative integrated intensity of the characteristic diffraction peaks [14]. The mol% of the monoclinic phase M_m and tetragonal/cubic phase $M_{t,c}$ in a system containing monoclinic, tetragonal, and cubic phases were calculated using [15, 16]:

$$\frac{M_m}{M_{t,c}} = 0.82\frac{I_m(11\bar{1}) + I_m(111)}{I_{t,c}(111)} \tag{1}$$

$$M_m + M_{t,c} = 100 \tag{2}$$

where $I_m(11\bar{1})$ and $I_m(111)$ are the X-ray diffraction intensities reflected from the $(11\bar{1})$ and (111) planes of *m*-phase, respectively, and $I_{t,c}(111)$ is the diffraction intensity reflected from the (111) planes of the *t*- and *c*-phases. This study was designed to study the effect of co-dopant on the stability of high-temperature phases (*c* and *t*), rather than to quantify *t*- and *c*-phases. Therefore, the mol% for *c*- or *t*-phase was not differentiated.

A Rigaku™ XRD with a CuK$_\alpha$ radiation source ($\lambda = 0.1542$ nm) was used. The X-ray scan was taken in the range $2\theta = 20$–100° at a scan rate of 0.8°/min. The X-ray peak identifications and intensity calculations were carried out employing a Jade™ 3.0 software package.

Differential scanning calorimetry (DSC) was used to study the phase transformation of the sintered samples during subsequent thermal cycles. DSC analysis involved the detection of changes in enthalpy of a sample with increasing or decreasing temperature using Y_2O_3 as a reference material. A Netzsch DSC 404C Pegasus calorimeter (Netzsch-Geratebau GmbH, Germany) was used. The weight of the samples for DSC analysis was set to be 35–45 mg and all the samples were ultrasonically cleaned and blow-dried prior to test. In each DSC run, the temperature was increased from 100 to 1,400 °C at a heating rate of 20 °C/min. Samples were held at 1,400 °C for 5 min, the temperature was then decreased from 1,400 to 400 °C at a cooling rate of 50 °C/min to examine the effect of faster cooling.

Results and discussion

SEM analysis of the as-sintered samples

The particle size and morphology of the mechanically alloyed powder material are shown in Fig. 1. Powder particle sizes are of several micrometers in diameter in contrast to 30 nm particle size for powders obtained by co-precipitation [17]. The surface morphologies and cross-sectional microstructures of the sintered materials in the etched condition were examined using SEM and illustrated in Figs. 2 and 3. As shown in Fig. 2, all samples exhibited sufficient consolidation after 120-h sintering at 1,500 °C. 5CeYSZ and 7NbYSZ assumed smoother surface morphologies and well-defined grain structures on the as-sintered surface, while the other samples revealed some porous surface features. Microstructural examination of the cross sections (Fig. 3) illustrated similar results in terms of the extent of sintering and the presence of porosities. Grain size measurement was carried out on the cross sections of the sintered samples using image analyzer, with the results summarized in Table 3. The grain sizes, ranging from 3 to 8 μm, were comparable to that reported in the literature where YSZ co-doped with Ta_2O_5 assumed a typical grain size of 5 μm after sintering at 1,500 °C for 120 h, despite the use of co-precipitated powders [18]. This indicates that the initial powder size does not have a direct impact on the final grain size which is primarily determined by the sintering condition.

The density values of the sintered samples were measured and are given in Table 3. A wide range of density values, from 86 to 95%, was observed. Overall, the densities were greater than the typical value for air plasma sprayed coatings [19] but lower than the reported values of 94–99% for sintered materials with powders obtained by

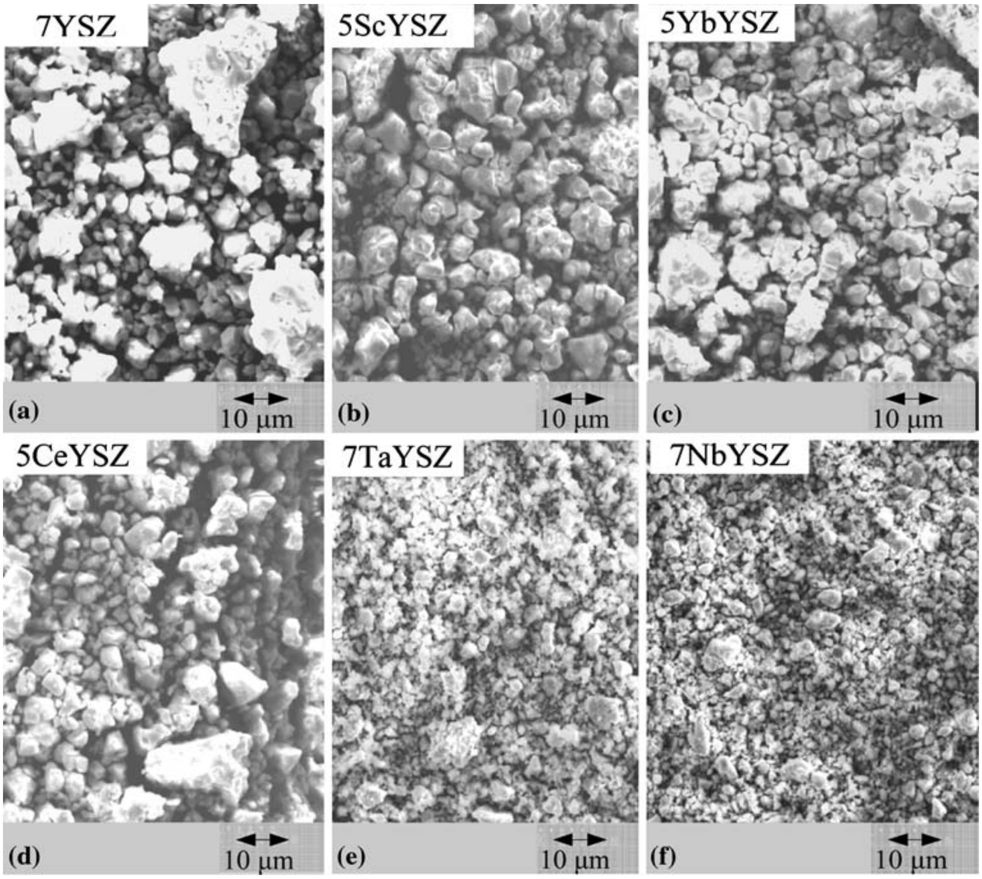

Fig. 1 Morphologies of the alloyed powders after 50 h grinding

co-precipitation [20]. The reduced densities found in this study are likely due to large powder size after mechanical alloying, affecting the packing density of the green compact. Elemental mapping was also carried out on the polished surfaces and confirmed the uniform distributions of co-dopant cations in the sintered samples.

Phase composition analysis

To analyze the phases present at room temperature after furnace cooling from 1,500 °C, XRD patterns were obtained for the polished samples as shown in Figs. 4 and 5. A summary of the calculated phase compositions is given in Table 2.

7YSZ

The sintered 7YSZ (3.9 mol% Y_2O_3) consists of both *m*-phase and *c*-phase at room temperature (Fig. 4). The molar percentage of *m*-phase, calculated using Eqs. 1 and 2, is about 46 mol% and the remainder is believed to be primarily *c*-phase since a strong *c*(200) peak can be identified from Fig. 4. Traces of *t*-phase may also exist since a small *t*(004) peak is discernable to the left of *c*(400). The equilibrium molar percentages of *c*- and *m*-phase for 7YSZ were estimated to be 31 and 69 mol%, respectively, from the Y_2O_3–ZrO_2 binary phase diagram at room temperature [10]. The reduced amount of *m*-phase in sintered 7YSZ indicated the non-equilibrium nature of the furnace cooling used in this study.

However, the amount of *m*-phase in the sintered 7YSZ is still higher than that observed in 3.9 mol%Y_2O_3–ZrO_2, which contained 32 mol% *m*-phase, after furnace cooling from 140-h aging at 1,400 °C [21]. While both grain size and density were not detailed in [21], the finer powder obtained from sol–gel would be expected to result in increased density. The increased amount of *m*-phase in 7YSZ can be attributed to the lower sintering density and larger grain size, both of which have been identified to have a significant impact on the extent of phase transformation from $t \rightarrow m$. In particular, the phase transformation temperature Ms ($t \rightarrow m$) increases with grain size [22] and porosity [23]. From a thermodynamic point of view, the change in free energy from $t \rightarrow m$ reduces as the strain energy and surface energy associated with *m*-phase formation are decreased. A porous structure allows more

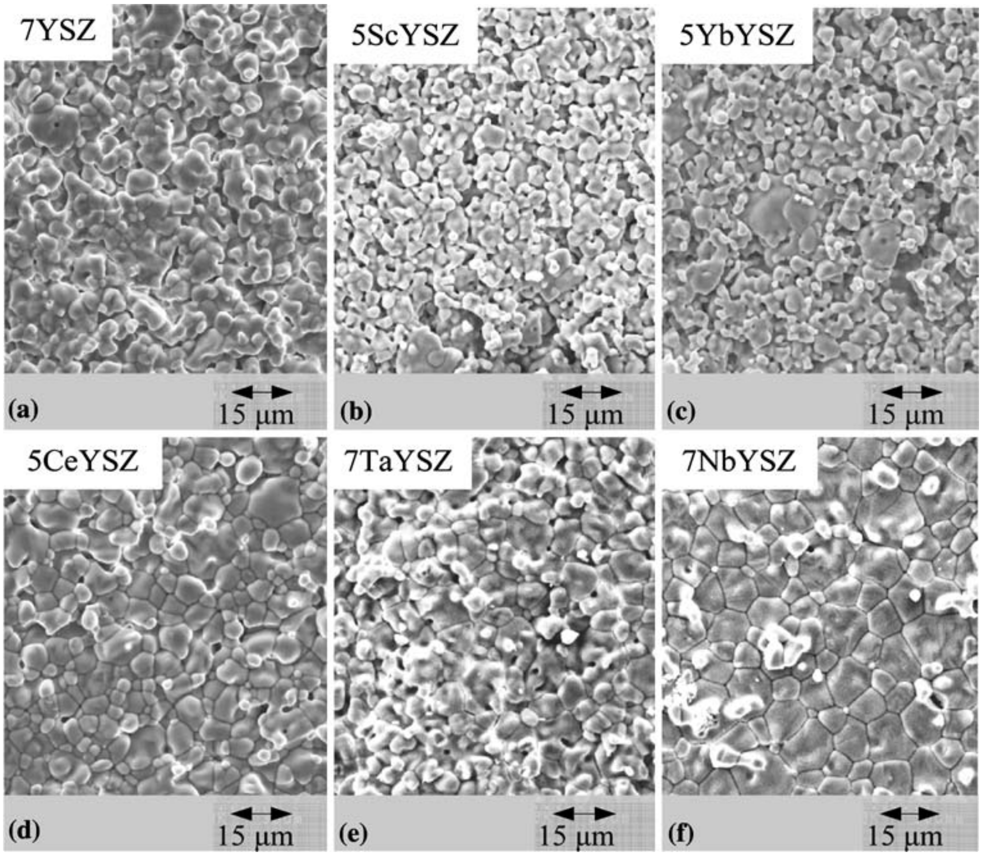

Fig. 2 Surface morphologies of sintered samples

Fig. 3 Cross-sectional microstructures of the sintered samples

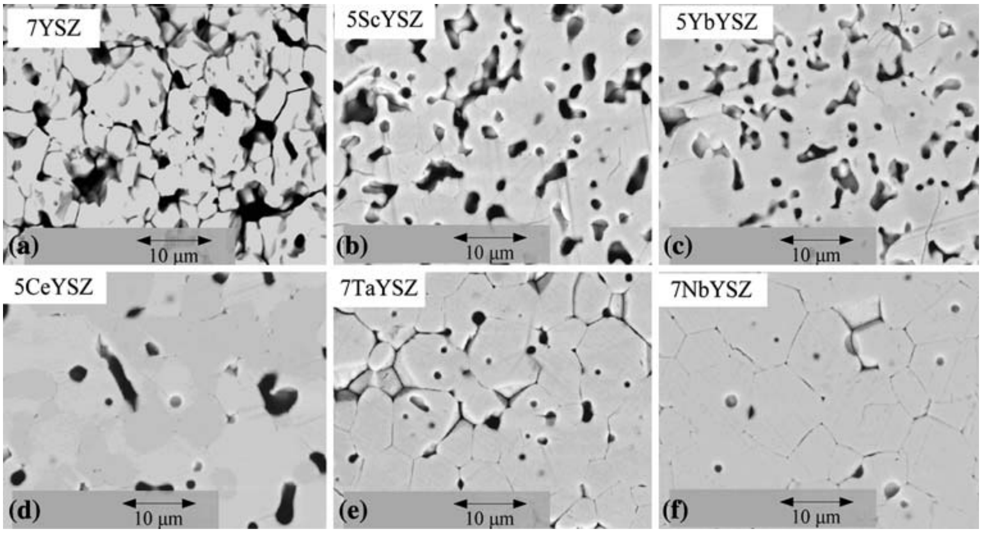

strain relaxation (since $t \rightarrow m$ accompanies volume increase), while a larger grain size has low resistance to the extension of *m*-phase from one grain to another [24].

Other factors that could contribute to the *m*-phase formation during cooling from sintering include sintering temperature, mol% of Y_2O_3 [18], and cooling rate [25]. Assuming equilibrium conditions are achieved during sintering, and based on the binary phase diagram [24], a lower sintering temperature or a higher mol% of Y_2O_3 reduces the amount of *t*-phase at sintering temperature, hence reducing the subsequent transformation to *m*-phase during cooling. Based on the phase diagram, a lower sintering temperature also increases the mol% of Y_2O_3 in the *t*-phase, leading to a reduced Ms [22] and lesser *m*-phase.

Table 3 Grain size and volume percentage of porosity in the sintered samples

Sample ID	Grain size range (μm)	Average grain size (μm)	Density (vol%)
7YSZ	1–6	4.3	87
5ScYSZ	1–4	3.0	97
5YbYSZ	1–6	3.0	86
5CeYSZ	2–10	4.6	95
7TaYSZ	3–10	8.0	91
7NbYSZ	3–15	6.7	95

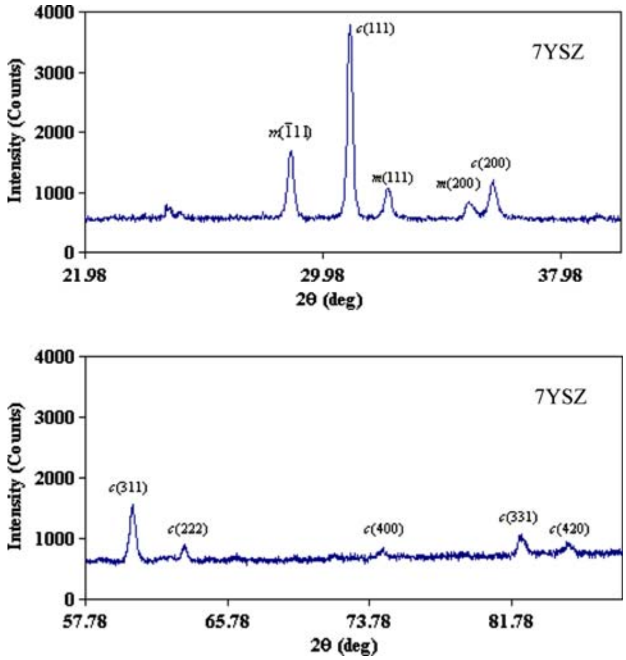

Fig. 4 XRD patterns of 7YSZ

The effect of cooling has also been investigated [25], where it was found that furnace cooling (10 °C/min) after aging at 1,482 °C for 100 h resulted in ~30 mol% *m*-phase in 8YSZ but faster cooling after the same aging cycle caused very little *m*-phase.

Lastly, for similar compositions, higher process temperatures in the *c*-phase region or molten state were able to retain high-temperature phases. Examples include SX 7.7YSZ (4.2 mol% Y_2O_3) cooled from skull melting contained a mixture of *t*-precipitates within a *c*-phase matrix [26]; the 12 mol% *m*-phase in 7YSZ plasma spray powder was eliminated after thermal spraying due to the higher spraying temperature and possibly faster cooling rate [27]. Despite the lack of grain boundaries in SX YSZ, the matrix surrounding the *t*-precipitates provided constraint to the volume increase associated *t* → *m* and effectively stabilized the *t* phase.

5ScYSZ and 5YbYSZ

Sample 5ScYSZ consists of 94 mol% of *c*-phase and a small amount of *m*-phase (6 mol%), while 5YbYSZ contains 100 mol% *c*-phase, as determined from the XRD patterns shown in Fig. 5a, b and summarized in Table 4. The addition of 2.5 mol% Sc_2O_3 to 7YSZ increased the amount of *c*-phase from 54 to 94 mol% due to the increased vacancy content from the addition of trivalent co-dopant [28]. The mol% of *c*-phase was further increased to 100 mol% with the addition of 2.5 mol% Yb_2O_3. Examining the ternary phase diagram of ZrO_2–Y_2O_3–Yb_2O_3 at both 1,400 and 1,650 °C [17] indicated that upon reaching equilibrium, 5YbYSZ assumed 100% *c*-phase at 1,500 °C; the 100% *c*-phase in 5YbYSZ was retained to room temperature despite the slow furnace cooling. This result is consistent with another study in which 10 mol% of $Y_2O_3 + Yb_2O_3$ in ZrO_2 effectively stabilized 100% *c*-phase [17]. Since Sc^{3+} has a smaller ionic radius than Yb^{3+}, it has a lesser influence in increasing the lattice parameters of the crystal [29] and consequently less stabilizing effect on the *c*-phase. While a ternary phase diagram for ZrO_2–Y_2O_3–Yb_2O_3 was not consulted at this time, it is reasonable to assume that 5ScYSZ fell within a *t*- + *c*-phase region during sintering at 1,500 °C. Dopants to zirconia with smaller ionic radius (such as Sc^{3+}) also have the effect of increasing Ms (*t* → *m*) than larger ions (Y^{3+}, Sm^{3+}) with the same dopant concentration [13]. Both factors have contributed to the occurrence of *m*-phase in 5ScYSZ upon cooling. Although the oxygen vacancy concentrations in 5ScYSZ and 5YbYSZ are identical, the phase stability of 5YbYSZ is greater than 5ScYSZ in terms of both *c*-phase retention and *m*-phase formation. Since 5ScYSZ has same grain size as 5YbYSZ and higher density, the high density could have only helped to stabilize the *t*-phase.

It is to be pointed out that there is a small diffraction peak seen at $2\theta = 44.5°$ on the XRD spectrum for 5YbYSZ. It is not certain what the nature of this phase is and will require further study.

5CeYSZ

The XRD pattern for 5CeYSZ is quite different from the others, as shown in Fig. 5c. It indicates the presence of a very small amount of *m*-phase (2.5 mol%) and a large percentage of *t*- and *c*-phase (97.5 mol%) mixture. It is difficult to speculate the possible effect of Ce^{4+} on stabilizing *c*-phase since the exact amount of *c*-phase in the *t*- + *c*-phase mixture was not determined in this study. However, it is certain that Ce^{4+} has an impact on the stabilization of *t*-phase since distinct *t*(002) and *t*(200) peaks were observed on the XRD pattern for 5CeYSZ while none

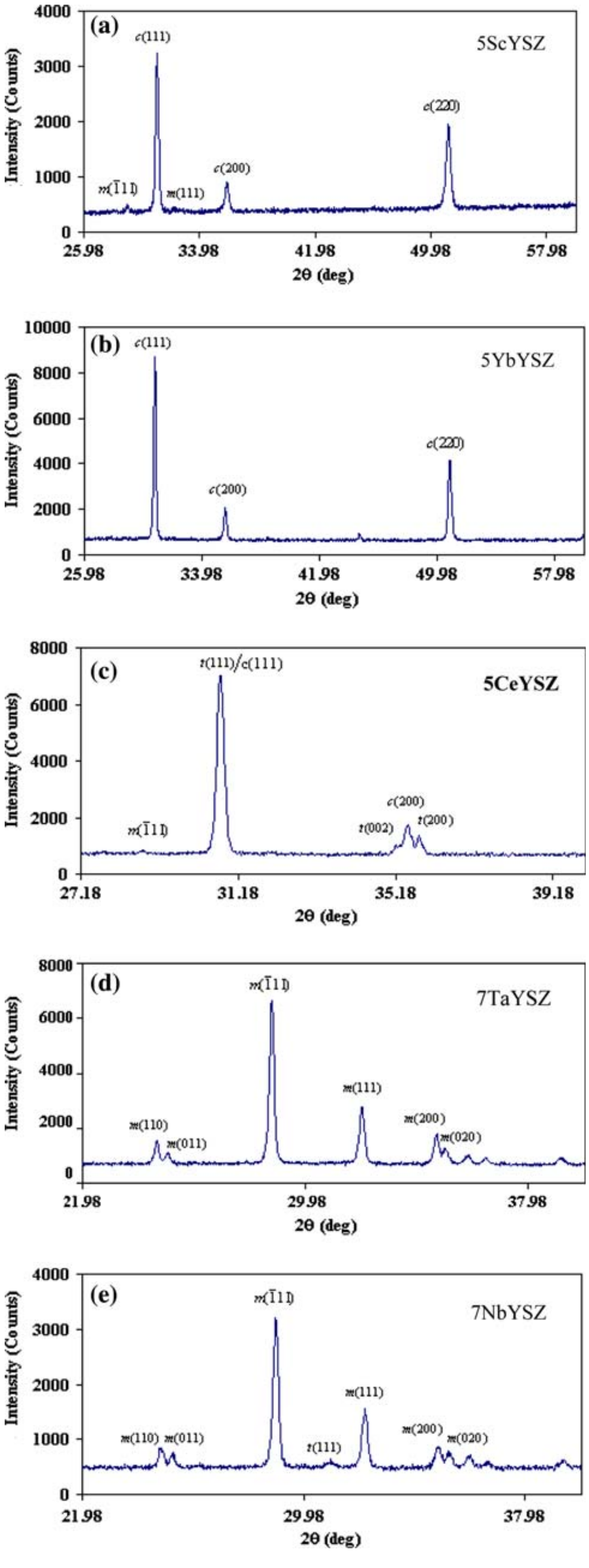

Fig. 5 XRD patterns of the co-doped samples

Table 4 The mol% of *m*- and *t*-, *c*-phases for the as-sintered samples

Sample ID	M_m (mol %)	$M_{t,c}$ (mol%)
7YSZ	46	54 *c*
5ScYSZ	6	94 *c*
5YbYSZ	–	100 *c*
5CeYSZ	2.5	97.5 *t* + *c*
7TaYSZ	100	0
7NbYSZ	97	3 *t*

of these peaks were present on the XRD pattern for 7YSZ. Since the Ce^{4+} does not induce extra oxygen vacancies in 7YSZ, the stabilization effect on *t*-phase is attributed to the larger ionic radius and higher atomic mass of the substitutional Ce^{4+} ion in the ZrO_2 lattice. This is supported by a previous study in which the addition of 9 mol% CeO_2 to ZrO_2 alone was found to be able to stabilize 100% *t*-phase with grain size in the range of 1–3 μm and 94–97% density (similar to the density of 5CeYSZ) after sintering at a temperature range of 1,400–1,550 °C [30]. In general, it is believed that the addition of a cation with a larger ionic radius than Zr^{4+} can significantly stabilize the high-temperature *t*-phase, even though the degree of such stabilization may be less than that of oxygen vacancies [29]. This mechanism of stabilization can be attributed to the effect of CeO_2 addition on reducing Ms ($t \rightarrow m$) temperature [23]. Since no previous study on similar compositions as 5CeYSZ was found, the influence of grain size, density, and cooling on *m*-phase formation cannot be further commented.

7TaYSZ and 7NbYSZ

The XRD patterns for the sintered 7TaYSZ and 7NbYSZ are shown in Fig. 5d, e. 7TaYSZ contains 100 mol% *m*-phase while 7NbYSZ is comprised of 97 mol% *m*-phase and 3 mol% *t*-phase. The identification of the *t*-phase rather than *c*-phase in 7NbYSZ was based on the occurrence of a small *t*(111) peak at $2\theta = 31°$ on the XRD pattern shown in Fig. 5e. Additionally, the ternary phase diagrams show that both 7TaYSZ [18] and 7NbYSZ [12] assume single *t*-phase at the sintering temperature of 1,500 °C. The addition of pentavalent oxides such Nb_2O_5 and Ta_2O_5 to YSZ suppresses the oxygen vacancy and promotes the occurrence of *t*-phase (as opposed to the stabilization of *c*-phase by trivalent oxides discussed earlier) and subsequently encourages the formation of *m*-phase by increasing the Ms ($t \rightarrow m$) temperature [18].

Results from another study showed that 100% *t*-phase was measured for 10 mol% Nb_2O_5–10 mol% Y_2O_3–ZrO_2

(sample N5) and 10 mol% Ta_2O_5–10 mol% Y_2O_3–ZrO_2 (sample T13) after aging at 1,500 °C for 200 h [31]. Since no vacancy existed in samples 7NbYSZ, 7TaYSZ, N5, and T13, the differences in the phase compositions are as a result of the following factors: grain size, porosity level, and the total amounts of substitutional defects in the zirconia lattice structure. While the grain sizes for sample N5 and T13 after aging were not given, the densities for N5 and T13 were greater than 97.5% in contrast to 91.2 and 95% for 7TaYSZ and 7NbYSZ, respectively. The increased porosities in 7TaYSZ and 7NbYSZ could have contributed to the phase transformation from $t \rightarrow m$ during cooling [24, 32]. Also, it has been observed that the *m*-phase formation in ZrO_2–Y_2O_3–Nb_2O_5 system can only be avoided if the mol% for $YNbO_4$ is greater than 10 mol% [12]. This has been confirmed in systems with 4.3 mol% Y_2O_3–1.1 mol% Nb_2O_5 or 1.1 mol% Ta_2O_5–ZrO_2 where 10 and 32 mol% *m*-phase, respectively, were reported after sintering at 1,500 °C [20]. The smaller amount of *m*-phase in 7NbYSZ (compared to 7TaYSZ) and 4.3 mol% Y_2O_3–1.1 mol% Nb_2O_5–ZrO_2 (compared to 4.3 mol% Y_2O_3–1.1 mol% Ta_2O_5–ZrO_2) can be attributed to the smaller mass of Nb^{5+} (half of Ta^{5+}) and its influence on reducing Ms ($t \rightarrow m$) temperature. This is in agreement with that observed in other studies [20, 23]. The smaller grain size and higher density in 7NbYSZ, in comparison to 7TaYSZ, could also have contributed to the reduced Ms.

Phase transformation of sintered samples during heat and cooling

The DSC curves for the sintered samples upon heating from room temperature to 1,400 °C and cooling from 1,400 to 400 °C are shown in Figs. 6, 7, and 9. On DSC curves, endothermic (heat is taken in) and exothermic (heat is given out) peaks provide indications of possible phase changes. Additionally, since the specific heat of each material is a function of temperature, this will give rise to further fluctuations on the DSC curves. However, in this study the DSC curves were used primarily as a tool to indicate the occurrence of phase transformation and the temperature at which the transformation takes place.

7YSZ

From XRD results reported in Table 4, it is known that 7YSZ contains 46 mol% *m*-phase in addition to 54 mol% of *c*-phase. Observing the DSC curve in Fig. 6, it is found that a phase transformation occurs at about 621 °C (onset temperature) as indicated by the change in heat flux from the baseline. Since the low temperature *m*-phase is unstable upon heating, this phase transformation is represented by $m \rightarrow t$. With a further increase in temperature, the DSC curve does not show any further peak up to 1,400 °C. During the cooling cycle at a faster rate of 50 °C/min (compared to the cooling rate of 5°/min used in sintering), a reversed phase transformation corresponding to $t \rightarrow m$ is observed at 483 °C. This phase transformation temperature is much lower than that observed on the heating cycle due to the nature of the non-equilibrium cooling rate. There are no additional peaks observed below 483 °C.

5ScYSZ and 5YbYSZ

The DSC curves for samples 5ScYSZ and 5YbYSZ are shown in Fig. 7a, b. As determined using XRD, samples 5ScYSZ and 5YbYSZ contain 94 and 100 mol% *c*-phase,

Fig. 6 DSC heat (solid line) and cooling (dashed line) curves for 7YSZ

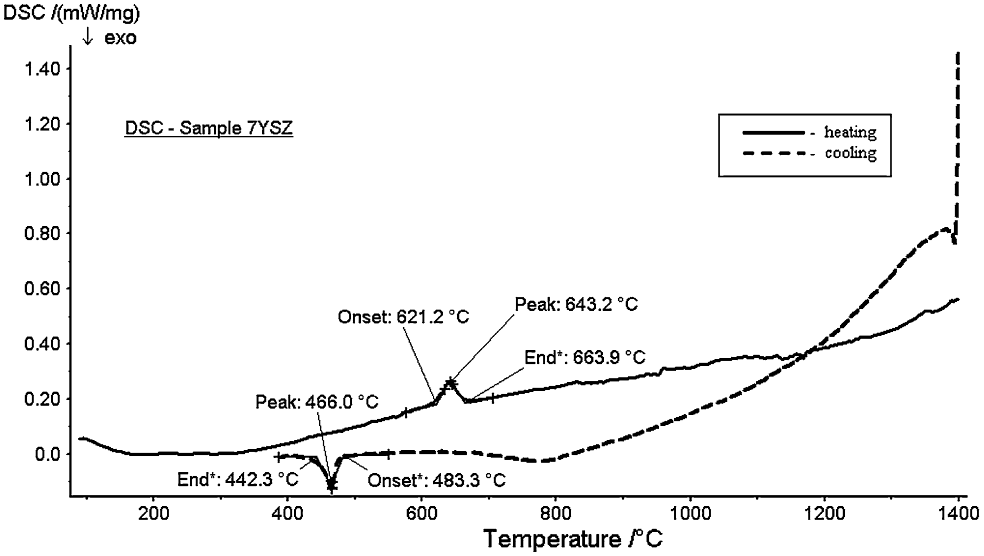

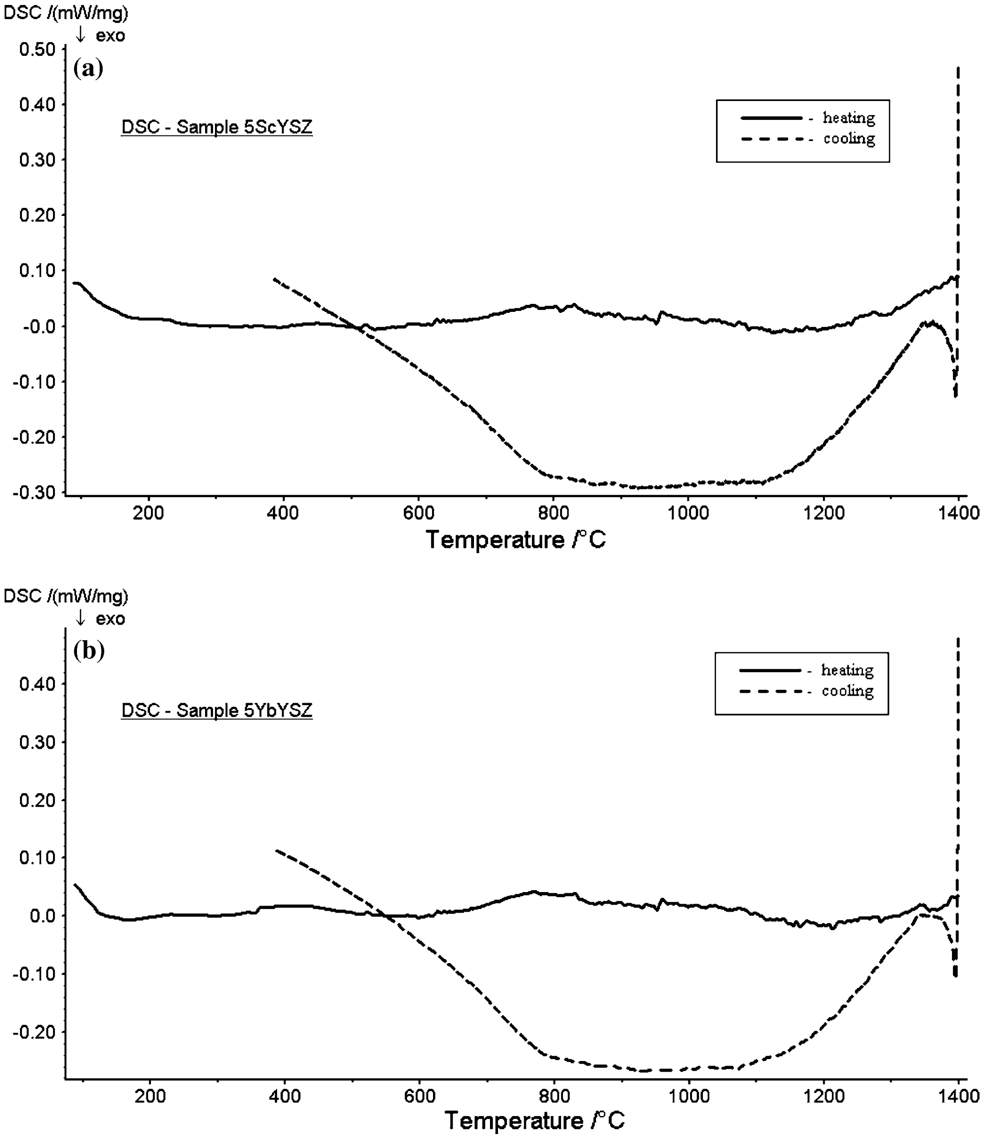

Fig. 7 DSC heating (solid line) and cooling (dashed line) curves: (**a**) 5ScYSZ and (**b**) 5YbNbYSZ

respectively. The DSC did not detect any phase change in 5ScYSZ during the heating cycle even though it contains 6 mol% of *m*-phase after sintering. This indicates the limited detection capability of the DSC facility. Upon cooling, there is no distinct peak to indicate phase transformation occurring; however, there is a valley observed on the DSC curve between the temperatures of 1,100 and 800 °C for both 5ScYSZ and 5YbYSZ, the nature of which has not been identified at the moment.

5CeYSZ

The sintered sample 5CeYSZ contains primarily *t*- and *c*-phases and limited amount of *m*-phase (2.5 mol%), as shown in Table 4. However, the phase transformation of *m* → *t* is not observed on the DSC curve. Upon cooling, no phase transformation can be identified from the DSC curve down to 400 °C as shown in Fig. 8.

7TaYSZ and 7NbYSZ

The DSC curves for 7TaYSZ and 7NbYSZ are shown in Fig. 9a, b. Upon heating, 7TaYSZ, with 100 mol% *m*-phase at room temperature, exhibits a phase transformation at 632 °C (onset temperature), indicating the phase transformation of *m*- → *t*-phase taking place at this temperature. During cooling, a phase transformation takes place at 522 °C (onset temperature) corresponding to *t*- → *m*-phase transformation. For sample 7NbYSZ, the transformation from *m* → *t* appears at a much lower temperature of 524 °C (onset temperature) as shown in Fig. 9b. When the temperature is further increased, another small deviation from the baseline

Fig. 8 DSC heating (solid line) and cooling curve (dashed line) for 5CeYSZ

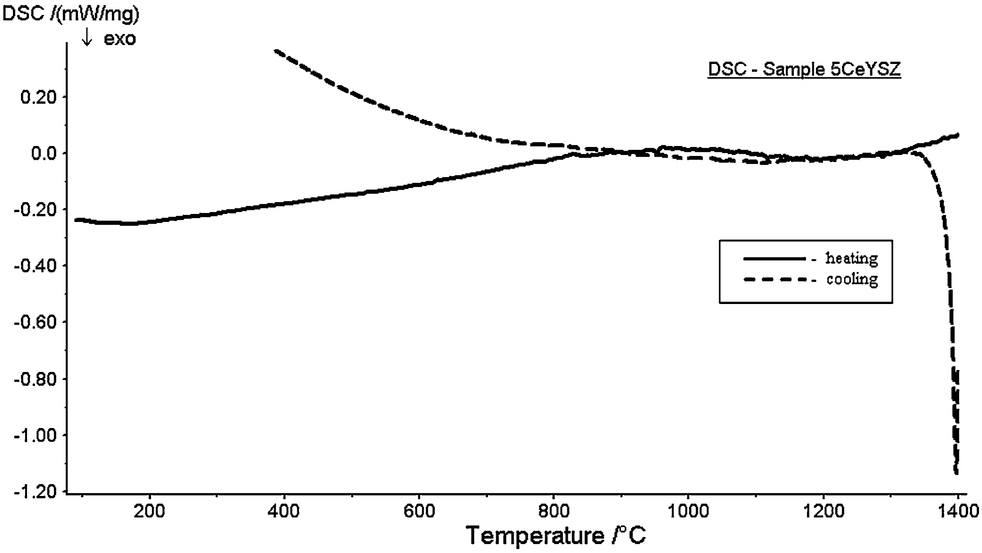

Fig. 9 DSC heating (solid line) and cooling (dashed line) curves: (**a**) 7TaYSZ and (**b**) 7NbYSZ

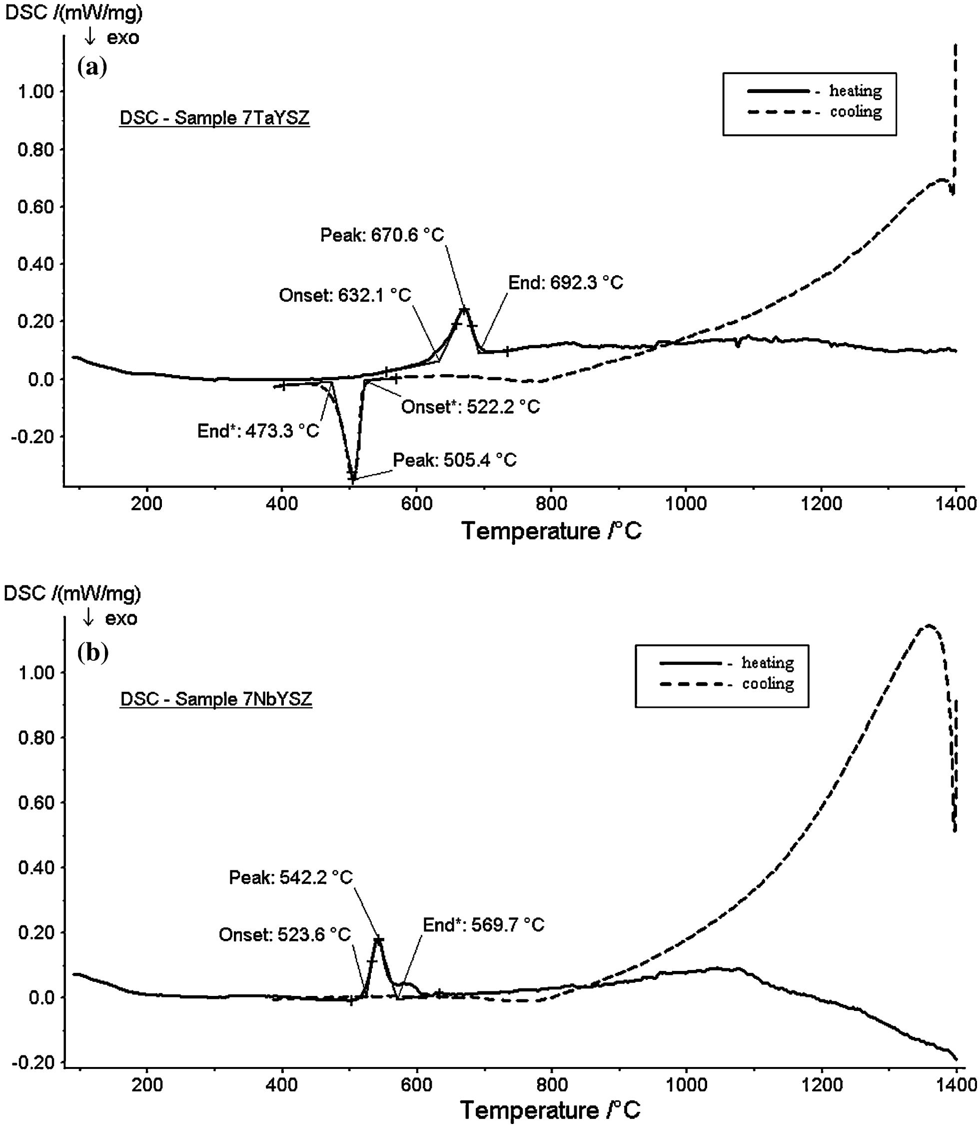

is observed at around 580 °C. The nature of this reaction is unclear. Unlike 7TaYSZ with an Ms ($t \rightarrow m$) temperature of 522 °C, 7NbYSZ does not exhibit this transformation of $t \rightarrow m$ before 400 °C during cooling, further confirming the effect of its smaller mass (Nb^{5+} has half the mass of Ta^{5+}), higher density, and smaller grain size on reducing Ms temperature. It is expected that the phase transformation from *t*- to *m*-phase will take place before reaching room temperature.

Conclusion

In this study, the microstructure and phase transformation of ternary zirconia-based oxides were studied. Ternary oxides were formed by doping 7YSZ with various metal oxides selected based on their specific valence, ionic radius, and atomic weight. Upon mechanical alloying and sintering at 1,500 °C for 120 h, homogeneous microstructures were obtained. The phase compositions were determined using XRD and the phase transformation during heating and cooling cycles was studied using DSC. While in general the oxygen vacancy has significant influence on the stabilization of high-temperature phases, other factors such as sintering temperature and time, cooling rate, grain size, and porosity all played important roles. It was found in this study that trivalent dopant cations help to stabilize *c*-phase while the tetravalent cations promote the formation and retention of *t*-phase to lower temperature. Larger trivalent cations (such as Yb^{3+}) play more roles in stabilizing high-temperature phases than smaller ions (such as Sc^{3+}). The additions of pentavalent cations to 7YSZ destabilize the high-temperature phases and increase the occurrence of *m*-phase upon cooling. It is also believed that cations with smaller atomic mass (Nb^{5+}) may offer more stabilization effect on the high-temperature *t*-phase by lowering the Ms.

Comparing the results obtained in this study to that reported in the literature, it is concluded that several factors can contribute to the final room temperature microstructure of doped or co-doped zirconia-based material; these being dopant type (valence, mass, and ionic radius), dopant concentration, initial powder size and shape (affecting the densities of the green compact and the sintered material), sintering temperature and time, and cooling rate.

As also observed in this study, both XRD and DSC have limited sensitivity to detect small fraction of phase changes. To overcome the disadvantage associated with the techniques, high-temperature neutron diffraction will be used in our further study to quantitatively evaluate the phase compositions during heating and cooling cycles.

Acknowledgement The authors would like to thank NSERC (Natural Science and Engineering Research Council) for providing a discovery grant (Grant No.: 261373-05) to Dr. Xiao Huang in supporting this research. The authors also acknowledge Drs. Q. Yang and Weijie Chen for their help with XRD and SEM.

References

1. Klemens PG (1990) Physica B 263–264:102
2. Jones RL (1996) In: Stern KH (ed) Thermal barrier coatings, metallurgical and ceramic protective coatings. Chapman & Hall, London, ISBN 0-412-54440-7
3. Bose S, DeMasi-Marcin J (1995) NASA CP3312:63
4. Levi CG (2004) Curr Opin Solid State Mater Sci 8:77
5. Sakuma T (1998) Key Eng Mater 153–154:75
6. Brandon JR, Taylor R (1991) Surf Coat Technol 46:75
7. Nicholls JR, Lawson KJ (2002) Surf Coat Technol 151–152:383
8. Zhu D, Chen YL, Miller RA (2002) J Am Ceram Soc 23(4):457
9. Wang D (2006) Ph.D. thesis, Carleton University, December
10. Scott HG (1975) J Mater Sci 10:1527
11. Michel D, Faudot F, Gaffet E, Mazerolles L (1993) J Am Ceram Soc 76(11):2884
12. Lee DY, Kim D-J, Cho D-H (1998) J Mater Sci Lett 17:185
13. Yashima M, Kakihana M, Yoshimura M (1996) Solid State Ionics 86–88:1131
14. Ladd MFC, Palmer RA (1994) Structure determination by X-ray crystallography. Plenum Press
15. Miller RA, Smialek JL, Garlick RG (1981) J Am Ceram Soc 3:241
16. Brandon JR, Taylor R (1991) Surf Coat Technol 46:75
17. Corman GS, Stubican VS (1985) J Am Ceram Soc 68(4):174
18. Kim D-J (1991) J Am Ceram Soc 74(12):3061
19. Raghavan S, Wang H, Dinwiddie RB, Porter WD, Mayo MJ (1998) Scr Mater 39(8):1119
20. Raghavan S, Wang H, Dinwiddie RB, Porter WD, Vaβen R, Stöver D, Mayo MJ (2004) J Am Ceram Soc 87(3):431
21. Jones R, Reidy R, Mess D (1996) Surf Coat Technol 86–87:94
22. Mayo MJ, Suresh A, Porter WD (2003) Rev Adv Mater Sci 5:100
23. Kim D-J (1990) J Am Ceram Soc 73(1):115
24. Chevalier J, Gremillard L, Deville S (2007) Annu Rev Mater Res 37:1
25. VanValzah JR, Eaton HE (1991) Surf Coat Technol 46:289
26. Mèvrel R, Laizet J-C, Azzopardi A, Leclercq B, Poulain M, Lavigna O, Demange D (2004) J Eur Ceram Soc 24:3081
27. Antou G, Montavon G, Hlawka F, Cornet A, Coddet C (2005) Ceram Int 31:611
28. Kuwabara A, Katamura J, Ikuhara Y, Sakuma T (2002) J Am Ceram Soc 85:2557
29. Kountouros P, Petzow G (1993) Science and technology of zirconia V. Technomic, Lancaster, Basel, p 30
30. Liu T, Mai Y-W, Swain MV (1994) J Mater Sci 29(3):835
31. Raghavan S, Wang H, Porter WD, Dinwiddie RB, Mayo MJ (2001) Acta Mater 49:169
32. Chen LB (2006) Surf Rev Lett 13(5):535